ACS APPLIED NANO MATERIALS

www.acsanm.org Article

$Ni(OH)_2$ Nanosheets Grown on Reduced Graphene Oxide for Supercapacitor Electrodes

Binglin Guo, Yihao Gao, Yongyue Li, Xin Sun, Shuailin Chen, and Meicheng Li*

Cite This: *ACS Appl. Nano Mater.* 2022, 5, 7471−7480 Read Online

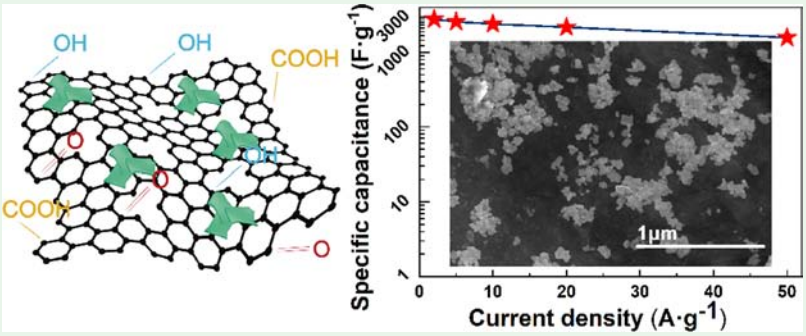

ABSTRACT: $Ni(OH)_2$ has low production cost and high theoretical specific capacity, while on account of the poor electronic conductivity, it shows inferior electrochemical performance including cycling stability and rate capability. This work focuses on a composite material that is *in situ* grown $Ni(OH)_2$ nanosheets on reduced graphene oxide (rGO), and employing the fewer-defect rGO to build a three-dimensional conductive network provides outstanding conductivity. The specific capacitances (C_m) of the $Ni(OH)_2$/rGO (NHG) electrode are 2776 $F{\cdot}g^{-1}$ at 2 $A{\cdot}g^{-1}$ and even 1570 $F{\cdot}g^{-1}$ at 50 $A{\cdot}g^{-1}$, demonstrating remarkable rate capability. It indicates that the combination of the nano grown $Ni(OH)_2$ and rGO conductive substrate shortens the ion diffusion path and increases the electron transfer rate; hence, the composite rate capability has been significantly improved. The composite materials and active carbon were combined to be an asymmetric supercapacitor, which had a high energy density of 39.24 $Wh{\cdot}kg^{-1}$ at 1962 $W{\cdot}kg^{-1}$. After 10,000 cycles at 5 $A{\cdot}g^{-1}$, the capacity retains 91.4%.

KEYWORDS: *$Ni(OH)_2$, supercapacitor, rate capability, energy storage, defects*

1. INTRODUCTION

Energy issues have severely restricted the development of human society. Fossil fuel usage is not only unsustainable, but it also seriously pollutes the environment and waste resources. Most renewable energy is ultimately stored and utilized in electric energy, which has led researchers to focus on developing high-performance and environment-friendly power storage devices. However, renewable energy has volatility, such as uneven spatial distribution of wind energy and uneven temporal distribution of solar energy. These require energy storage devices to have excellent rapid charge and discharge capability to cope with fluctuating energy supply. The performance of the electrode could affect the performance of the device to a large extent. Electrode materials can be divided into double-layer materials, pseudocapacitance materials, and battery-type materials by the mechanism of energy storage. Among them, the electric double-layer material is mainly based on physical adsorption and desorption during the charging−discharging process, which usually has a better cycle performance and smaller capacitance. Therefore, doping and modification are often used to increase its electrochemical performance.[1,2] Common materials are mainly porous carbon,[3,4] graphene, and its derivatives.[5] Pseudocapacitance and battery-type materials store energy by redox reaction, and the main difference between them is the solid-state diffusion controlling the chemical process of battery-type materials. Pseudocapacitance materials such as a conductive polymer,[6] metal organic framework,[7,8] and metal oxide[9−11] store electric charge based on fast Faradaic reactions that are not limited by solid-state diffusion.[12] The electrochemical reaction belongs to psedocapacitance behavior regardless of the bulk size of the materials. Typical examples of battery-type materials are $LiCoO_2$, $Ni(OH)_2$, and TiO_2. Such bulk battery materials show a predominant capacitance. The bulk redox reactions

Received: April 5, 2022
Accepted: April 13, 2022
Published: April 29, 2022

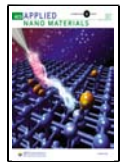

Scheme 1. Schematic Illustration of NHG Composite Material Synthesis[a]

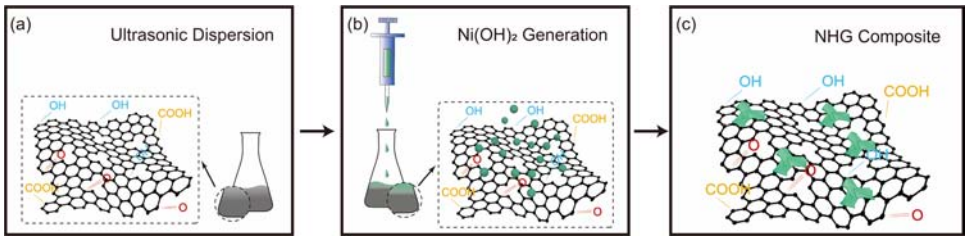

[a](a) Dispersion of GO in deionized water by ultrasonic. (b) Generation of $Ni(OH)_2$ on the surface of GO. (c) NHG composite obtained by the hydrothermal method.

were limited by mass transfer that leads to slow reaction dynamics, and electrochemical behavior has relevance with the bulk size of the material. A much bigger specific surface area of battery-type materials can be acquired, with the development of nanomaterials.[13−15] Thus, the ion diffusion distance was shortened obviously, so the bulk redox reaction is basically changed to surface redox reaction. Most of the redox sites grow on the interface of electrode−electrolyte and have more scattering than in bulk materials,[16−18] so the reaction dynamic can be faster than in bulk materials, which leads to a capacitor-like response of nanosize battery materials.[19,20] As mentioned, nanosize materials are so-called extrinsic pseudocapacitance materials, which show battery-like behavior in bulk redox reaction and capacitor-like behavior reducing the size to nanoscales.

As a battery-type material, $Ni(OH)_2$ is considered as a valuable energy storage electrode material for its high theoretical specific capacity, ease of acquisition,[21] and stable electrochemical behavior.[22−24] However, pure $Ni(OH)_2$ has a low electrochemical rate capability, which places restrictions on its further development in the energy storage scene.[25,26]

Nanomaterials and loading on high-conductivity substrates are effective ways to improve rate capability. The electrochemical performance of the $Ni(OH)_2$ electrode material needs to be improved urgently due to the tremendous limitation of solid-phase transfer mass in solid materials.[27] The low solid-phase transfer rate results in bulk $Ni(OH)_2$ being partly involved in reaction during high-rate charging and discharging, so its capacity is significantly lower than that of low-rate charging and discharging, which is the poor rate capability.[28] When the $Ni(OH)_2$ is reduced to a nanoscale, the ion diffusion path is significantly shortened and the electrode−electrolyte reaction interface is enlarged,[29] which effectively improves the utilization ratio and rate capability of the active material.[30] At the same time, the addition of high conductive substrates is a promising method of improving the conductivity of the composite. Specifically, growing $Ni(OH)_2$ on high-conductivity materials to accelerate charge transfer can significantly enhance electrode electrochemical performance.[31] Benefiting from high electronic conductivity, high specific surface area, a wide variety of sources, and stable electrochemical properties, carbon-based materials are often applied to constructing three-dimensional conductive networks.[32] The graphene shows a two-dimensional sheet structure that creates plenty of active sites and a high specific surface area, leading to fast reaction kinetics, making it a suitable conductive substrate for improving the conductivity of composite materials.[33] Benefiting from the 3D conductive network formed by graphene, electrons can be exported at a high speed, thereby realizing an electrode material with high rate capability, when $Ni(OH)_2$ and graphene were combined to be a composition material by *in situ* growth.

In recent years, such composite materials have been reported by several studies. Li et al. synthesized N-enriched graphene (NG) mixed with a $Ni(OH)_2$ nanosheet hydrogel that featured a C_m of 896 $F{\cdot}g^{-1}$ at 0.5 $A{\cdot}g^{-1}$ as well as 504 $F{\cdot}g^{-1}$ at 12 $A{\cdot}g^{-1}$ since the large specific surface area of NG improved electron transfer, and the N-doped sites were strong bonding sites for the metal hydroxide growth.[34] Combining NiFe LDHs (layered double hydroxides) with NF, Li et al. prepared a new 3D composite material that displayed a C_m of 1462.5 $F{\cdot}g^{-1}$ at 5 $A{\cdot}g^{-1}$ and about 64.7% in retention of the initial capacity after 2000 cycles with the rGO providing easy electron-transfer access.[35] Lai et al. synthesized a flower-like NHG electrode, which had a high surface area and performed a C_m of 1670.4 $F{\cdot}g^{-1}$ at a discharging current of 1 $A{\cdot}g^{-1}$.[36] The C_m of composite materials has been improved by these researches, but their rate capability is still unsatisfying.

We have combined $Ni(OH)_2$ with rGO to form NHG composite materials in this work (as illustrated in Scheme 1) for supercapacitor electrodes by a one-pot hydrothermal method using two kinds of GO as precursors (denoted by AGO and BGO). Among them, AGON, the composite material prepared from AGO, has high conductivity, in which the surface of AGO is evenly covered with $Ni(OH)_2$. Because of the high electronic conductivity of rGO, the electron of composites can be exported quickly, and the proton transfer rate can be raised by preparation of a nanosized $Ni(OH)_2$ sheet. The AGON performs a C_m of 2776 $F{\cdot}g^{-1}$ at 2 $A{\cdot}g^{-1}$ as well as 1570 $F{\cdot}g^{-1}$ at 5 $A{\cdot}g^{-1}$ in 6 M KOH solution. The AGON and active carbon were combined to be an asymmetric supercapacitor (ASC). When the power density is 1962 $W{\cdot}kg^{-1}$, the ASC stores a high energy density of 39.24 $Wh{\cdot}kg^{-1}$.

A preparation method of a high-performance composite electrode material has been reported. The use of this electrode material will effectively improve the electrochemical performance of the asymmetric capacitor. These high rate capability and high capacity devices have not only practical significance in the field of energy storage but also a reference value for more complex systems such as photovoltaic-storage integrated devices. At the same time, the relationship between the defects of the substrate (rGO) of the composite and the electrochemical performance has been noticed. The changes of the substrate in the process of preparing the composites and its role in the composite should be paid more attention to in further research.

https://doi.org/10.1021/acsanm.2c01464
ACS Appl. Nano Mater. 2022, 5, 7471−7480

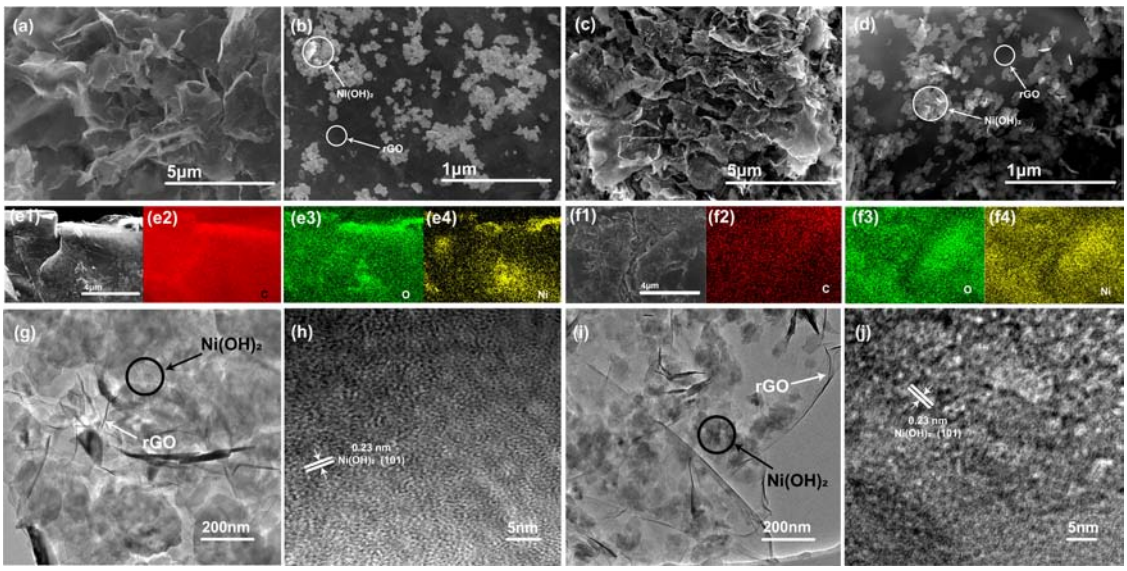

Figure 1. SEM, TEM, and HRTEM images of (a, b, g, h) AGON and (c, d, i, j) BGON at different magnifications. Elemental mapping of AGON (e) and BGON (f).

2. EXPERIMENTAL SECTION

2.1. Synthesis of the $Ni(OH)_2$/rGO Composite. AGO (0.1 g, ALADDIN) or BGO (XFNANO) was evenly dispersed in 100 mL of deionized water using an ultrasound probe sonicator for 180 min to obtain a proper suspension at room temperature. A certain amount of $NiSO_4{\cdot}6H_2O$ was dissolved in the suspension and left to stand for 60 min. Then, 20 mL of NaOH aqueous solution was added dropwise to form $Ni(OH)_2$ and GO suspension and held under blending for half an hour. The mixture was placed in a 175 mL polytetrafluoroethylene-lined stainless steel autoclave. Then we set them up for a hydrothermal reaction at 180 °C for 6 h. When the prepared samples were naturally cooled down, the sediment left was collected by centrifugation. Before the pH value of the filtrate became neutral, the samples were continuously washed with deionized water and absolute ethanol. At the last part of the experiment, the prepared samples were placed in a freeze-drying oven for 12 h and labeled as AGON and BGON, respectively.

2.2. Electrode Fabrication. The active material (AGON, BGON, or AC), PTFE, and acetylene black were prepared, weighed, and then mixed in a mass ratio of 82.5:7:10.5 and dispersed with absolute ethanol. The slurry was evenly spread on a nickel foam. The loaded nickel foam was then subjected to a 10 MPa pressure. During 12 h at 60 °C in a vacuum, the electrode was finally successfully prepared.

2.3. Electrochemical Measurements. The electrochemical test was completed in a standard three-electrode configuration, and the reference electrode in this work was the Hg/HgO electrode. The platinum foil and NHG composite material served as a counter electrode and working electrode, respectively, and the electrolyte in this work was 6 M KOH. The cyclic voltammetry (CV) tests were performed on AGON and BGON. The scan speeds changed within the 0−0.55 V potential range. The galvanostatic charging and discharging (GCD) curves under various current densities were measured between 0 and 0.5 V. Meanwhile, the formula of estimating the specific capacitances (C_m) of the electrodes was given as below

$$C_m = \frac{i\Delta t}{\Delta V} \tag{1}$$

Based on the GCD curve, the constant current density ($A{\cdot}g^{-1}$) was denoted by i, the entire discharge time (s) was denoted by Δt, and the working potential window was denoted by ΔV. The EISs of AGON and BGON were tested in the frequency range of 100 kHz to 0.01 Hz at the open circuit potential (OCP). All the electrochemical measurements were performed on an electrochemical workstation (CHI660E, Chenhua).

2.4. Assembling of an Asymmetric Cell. An ASC was assembled with AC, and AGON/BGON acted as the positive electrode. The recorded results of the battery test equipment (CT2001A, Land) reflected the cycle performance of the ASC. According to the conservation of charge, the mass ratio of the active material on the positive and negative electrode was calculated in eqs 1 and 2

$$q_+ = q_-$$

$$q = C_m \times m \times \Delta V$$

$$\frac{m_+}{m_-} = \frac{\Delta t_-}{\Delta t_+} \tag{2}$$

where $C_m i$ represents the specific capacitances of individual electrodes ($F{\cdot}g^{-1}$) and m_+/m_- represents the mass ratio of the positive and negative electrode active material.

The equations that estimate the energy density (E) and power density (P) of the ASC are shown in eqs 3 and 4

$$E = \frac{I \times \int V dt}{m} \tag{3}$$

$$P = \frac{E}{t} \tag{4}$$

where the constant discharge current (A) based on the GCD curve was denoted by I, the galvanostatic discharge curve area was denoted by $\int V dt$,[37] the total mass of active materials (kg) was denoted by m, and the full discharge time (h) was denoted by t.

2.5. Characterization Methods. Scanning electron microscopy (SEM, SU8100, HITACHI) and transmission electron microscopy (TEM, HRTEM, F20, FEI) were used to analyze the morphology and microstructure of the materials. With Cu Kα radiation at a scan rate of 5 °·min^{-1}, powder X-ray diffraction (XRD, D8 Focus, Bruker) was performed to measure the crystallographic information of the materials. Raman spectra were recorded in a Via-Reflex spectrometer (Renishaw). An ESCALAB 250 Xi system (Thermo Fisher) was used to perform the X-ray photoelectron spectroscopy (XPS) measurements utilizing monochromatic Al Kα X-ray. The actual loading of nickel hydroxide was tested by a simultaneous thermal analyzer (NETZSCH STA 449F3) under air conditions with a heating rate of 10 K·min^{-1}. Specific surface area and pore size distribution were measured by a Micromeritics ASAP2020 analyzer. The pore size

https://doi.org/10.1021/acsanm.2c01464
ACS Appl. Nano Mater. 2022, 5, 7471−7480

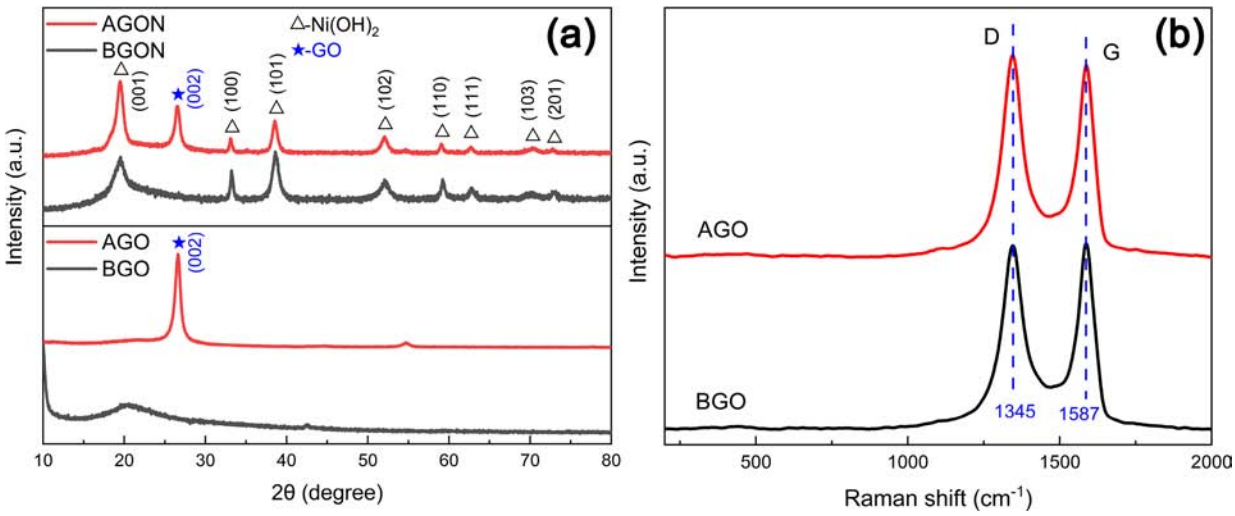

Figure 2. (a) XRD patterns of AGO, BGO, AGON, and BGON. (b) Raman spectra of AGO and BGO.

distribution curves were calculated by Barrett–Joyner–Halenda (BJH) adsorption branches.

3. RESULTS AND DISCUSSION

The two kinds of composites prepared by the hydrothermal method with $NiSO_4{\cdot}6H_2O$ as the nickel source and rGO as a conductive carrier were observed by SEM. In the preparation process, nickel ions are uniformly adsorbed on the surface of GO precursors rich in some oxygen-containing functional groups (OCFGs) as active sites by electrostatic action. Under high temperature and pressure, the hydrothermal reaction system has a strong Brownian motion, which leads to the formation of Ni–O bonds and the appearance of sheet structures. As shown in Figure 1, $Ni(OH)_2$ sheets both in AGON and BGON composites are well bonded with the carbon frame, indicating that rGO can be used as a substrate for *in situ* growth of $Ni(OH)_2$ sheets. There are a sheet-like distribution of $Ni(OH)_2$ and a part of the exposed rGO on the surface of AGON. Conversely, $Ni(OH)_2$ nanosheets in BGON are evenly distributed with a similar size and diameter of about 100 nm. The $Ni(OH)_2$ particles on the surface of AGON are piled one above another while that of BGON is more uniform. The stack of $Ni(OH)_2$ is much clearly observed in the TEM image, as shown in Figure 1g,j. The stack of $Ni(OH)_2$ particles formed a shadow, and the drape part is rGO. The HRTEM images of both materials show some clear lattice fringes with an equal interplanar distance of about 0.23 nm corresponding to (101) planes.

As a carbon-based 2D crystal, graphene has a single atomic layer thickness, and the carbon atoms are tightly bonded in a sp^2 hybrid manner to form a honeycomb lattice network.[38] As a derivative of graphene,[39] GO is based on a layer of graphite oxide.[40] Compared with the original graphene, on the one hand, the OCFGs in GO can produce significant structural defects, accompanied by some loss of conductivity.[41] On the other hand, these OCFGs can be employed as active sites for chemical modification or functionalization to immobilize various electroactive substances, providing potential advantages for the application of GO in electrochemical systems. GO can support active materials and promote electron transfer on the electrode surface due to its favorable electron mobility and abundant surface properties, such as single-atom thickness and high specific surface area.[42]

The XRD patterns of AGO, BGO, AGON, and BGON are shown in Figure 2a. The (002) crystal plane of the graphite structure corresponds to the peak of AGO at 26.5°. Relevantly, the expanding and shifting of the characteristic diffraction peak of BGO are mainly due to more OCFGs and defects of the carbon frame and enlarged lattice spacing. The diffraction peaks of AGON and BGON at approximately 19.2, 33.0, 38.5, 52.0, 59.0, 62.7, 70.3, and 72.7° correspond, respectively, to the (001), (100), (101), (102), (110), (111), (103), and (201) planes of β-$Ni(OH)_2$. Compared with the standard card (JCPDS: 14-0117), it confirms that the $Ni(OH)_2$ in composites is a high-purity β-phase crystal, which is consistent with the literature.[43,44] The GO peak of BGON could be masked by the high nickel hydroxide peak.

The content of defects and the degree of disorder in AGO and BGO are characterized by Raman spectroscopy in Figure 2b above. The D and G bands of two GO precursors can be reflected in two obvious peaks located at 1345 and 1587 cm^{-1}. Generally speaking, the D band is mainly caused by the sp^3 hybridization carbon atoms or the defects, which are related to the edge of the carbon frame and doping elements, whereas the G band is related to the vibration of sp^2 hybridization carbon atoms on the hexagonal lattice of graphene.[45−47] The ratio of the area of the D and G bands (I_D/I_G) can theoretically be used to determine the defect content of materials.[29] The ratios of I_D/I_G for AGO and BGO are 1.34 and 1.39, respectively, implying a higher degree of disorder for BGO.

The full-survey scan XPS spectra of AGO and BGO are shown in Figure 3a. Based on the C 1s peak, the intensity of the O 1s peak for AGO is significantly lower while that of BGO is the opposite. To characterize the difference of OCFGs on the surface of AGO and BGO, XPS spectra with high resolution are fitted. Figure 3b and Figure 3c show the C 1s spectra of AGO and BGO with their fitting results, respectively. Tables 1 and 2show the specific data. In terms of C–C in GO precursors, the content of OCFGs in BGO is as high as 58.8%, which is visibly higher than that in AGO (28.76%). In general, rGO is composed of hexagonal carbon networks with sp^2 hybridization carbon for the most part and sp^3 hybridization carbon for a small part.[48] For the ultrahigh electronic conductivity, the conjugated structure of sp^2 hybridization carbon atoms can effectively reduce the charge accumulation and bring about the uniform charge distribution

https://doi.org/10.1021/acsanm.2c01464
ACS Appl. Nano Mater. 2022, 5, 7471−7480

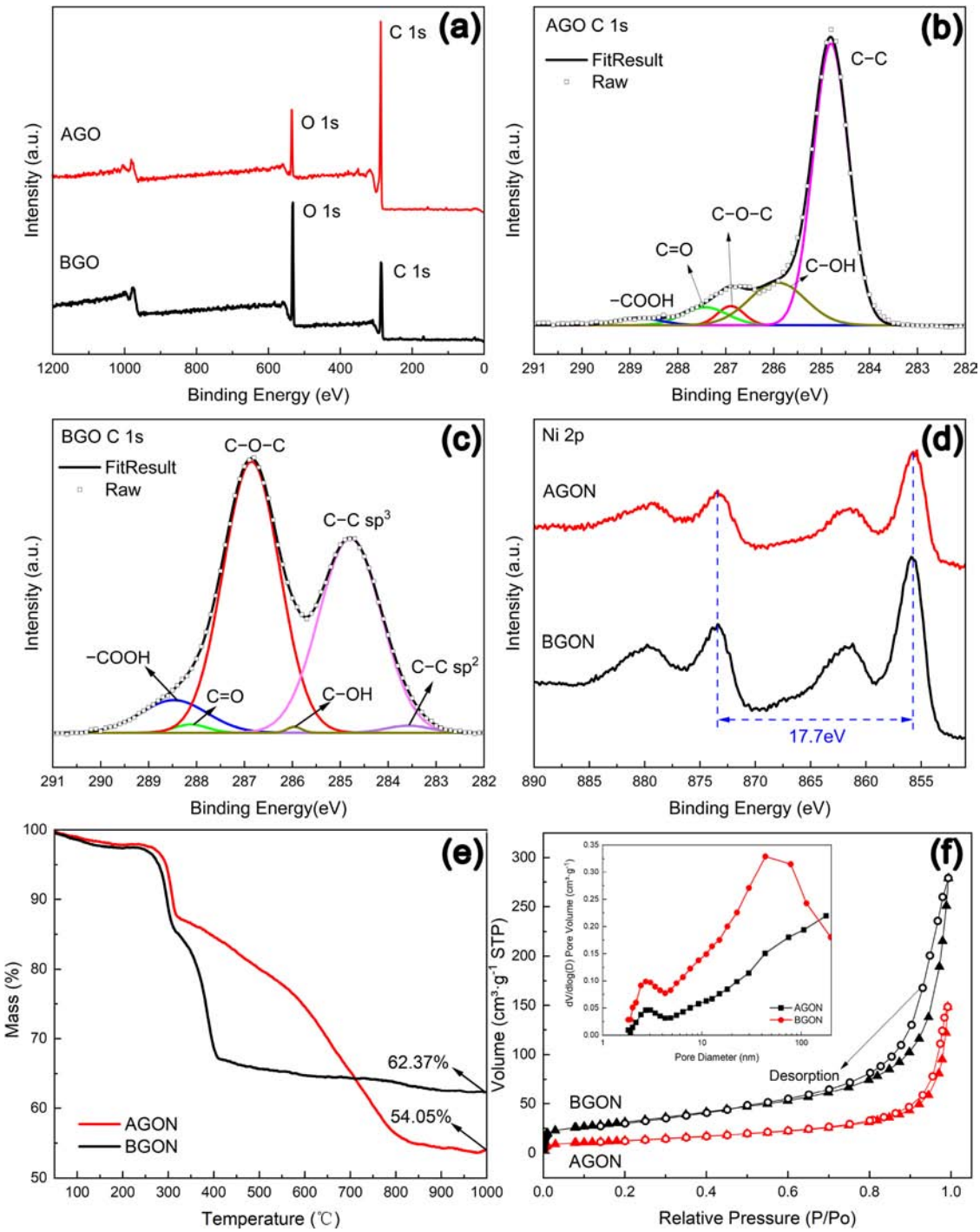

Figure 3. XPS spectra of AGO, BGO, AGON, and BGON: (a) survey scan. (b) C 1s of AGO. (c) C 1s of BGO. (d) Ni 2p of AGON and BGON. (e) TGA curve and (f) N_2 isotherm linear plot and pore size distribution (inset) of AGON and BGON.

Table 1. Deconvolution Result of the C 1s Spectrum of AGO

peak position (eV)	area (%)	band
288.8	2.30	−COOH
287.4	5.73	C═O
286.9	3.61	C−O−C
285.9	17.11	C−OH
284.8	71.24	C−C

Table 2. Deconvolution Result of the C 1s Spectrum of BGO

peak position (eV)	area (%)	band
288.5	7.18	−COOH
288.1	0.92	C═O
286.9	50.41	C−O−C
286.0	0.29	C−OH
284.8	40.15	C−C sp^2
283.6	1.05	C−C sp^3

https://doi.org/10.1021/acsanm.2c01464
ACS Appl. Nano Mater. 2022, 5, 7471−7480

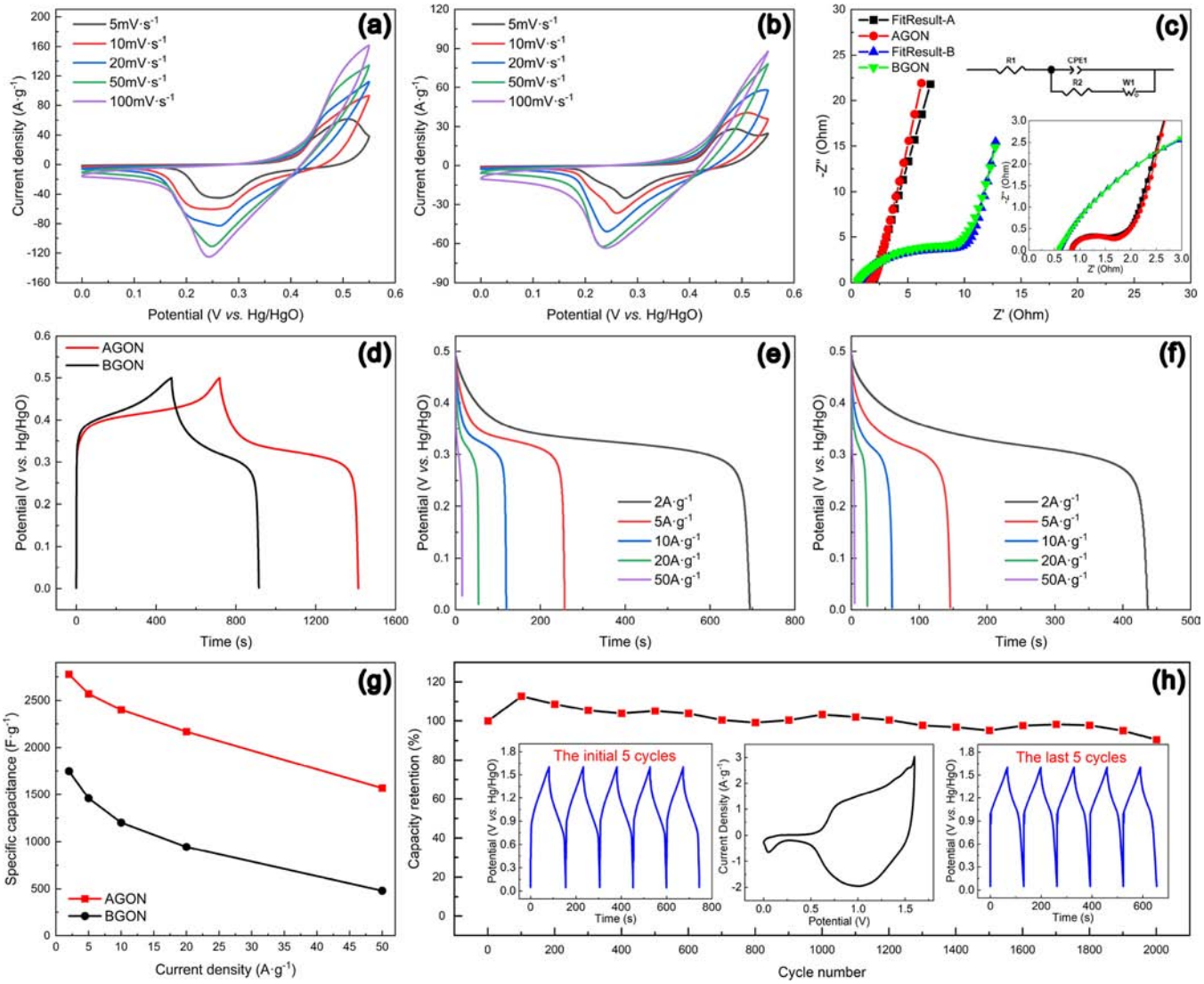

Figure 4. Electrochemical performance of the composite materials and ASC. CV of (a) AGON and (b) BGON at different scan rates. (c) Nyquist plots with fitting data of AGON and BGON, and the inset is the related equivalent circuit. (d) GCD curves of AGON and BGON electrodes at 2 $A \cdot g^{-1}$. GCD curves of (e) AGON and (f) BGON at different discharge rates. (g) Rate capability of AGON and BGON. (h) Stability of the ASC. Insets are the initial and last five cycles of GCD curves and the CV curve of the ASC.

on the surface of composite materials. The sp^3 hybridization carbon atoms, which are covalently bonded to the OCFGs, damage the original honeycomb structure and form defects, resulting in a decrease in the conductivity of materials.[49,50] According to existing research,[51,52] the OCFGs on the surface of GO precursors are usually employed as active sites during *in situ* growth. After mixing the nickel ions in the solution with GO precursors, the nickel ions rapidly adsorb on the surface of GO precursors through the electrostatic interaction with OCFGs. Then, the oxygen bridges are formed between nickel atoms and oxygen atoms for *in situ* growth. The higher content of OCFGs on the surface of BGO means that it can supply more reaction sites to *in situ* growth of $Ni(OH)_2$,[53,54] leading to abundant crystal nuclei to obtain more evenly distributed $Ni(OH)_2$ sheets.

The Ni 2p high-resolution spectra for AGON and BGON are similar, which is shown in Figure 3d. At 874.1 and 856.4 eV, there are two main peaks. Corresponding to Ni $2p_{1/2}$ and Ni $2p_{3/2}$, the spin energy separation in the Ni 2p XPS spectrum is 17.7 eV. The other two groups of peaks on the higher binding energy side are related to their satellite peaks, which is consistent with a previous report on the characteristics of $Ni(OH)_2$.[55]

The results of TG are shown in Figure 3e, which is calculated according to the fact that the end-products are NiO only when the test is completed. The remaining AGON is 54.05 wt %, which means 67.01 wt % of $Ni(OH)_2$ and 32.99 wt % of rGO in the composite material. The remaining BGON is 62.37 wt %, which means 77.41 wt % of $Ni(OH)_2$ and 22.59 wt % of rGO in the composite material. The corresponding values of BGON are 62.37, 77.41, and 22.59 wt %. There is more $Ni(OH)_2$ content in BGON, and the reason is that more OCFGs helped BGON adsorb more Ni^{2+}. Figure 3f shows the N_2 isothermal adsorption−desorption curve and pore size distribution. The N_2 isothermal adsorption−desorption curves of the two materials are type II curves, indicating that the low content of micropores of both two materials and the pore structure is relatively underdeveloped. The BET surface areas of AGON and BGON are 45.17 and 111.93 $m^2 \cdot g^{-1}$,

https://doi.org/10.1021/acsanm.2c01464
ACS Appl. Nano Mater. 2022, 5, 7471−7480

respectively. Within a pore width of 1−100 nm, the pore volume of BGON is also larger than that of AGON.

Figure 4a,b shows a clear and full redox peak of the CV curve at a low scan rate, which proves that the electrode reaction is adequate. The electrode process can be explained by the following equation:[56]

$$OH^- + Ni(OH)_2 \rightarrow NiOOH + H_2O + e^-$$

AGON has obvious redox peaks, indicating that the electrons and ions have fast transport speeds.[57] The well-reversible charge−discharge process of the electrode and the weak electrochemical polarization of the redox reaction lead to the close position of redox peaks in the CV curve. The reason is that the electrons can be exported quickly through the 3D conductive network formed by rGO, which significantly reduces the charge accumulation.[58] Compared to the BGON electrode, the redox peak of AGON is barely shifted during the increase in scan rate. This means that the request of diffusion rate can be met by the electrode material during the whole process of the scan rate increasing, which proves that the strategy of the composite electrode is effective.[59] The CV curve of AGON demonstrates a remarkably large enclosed area compared to the BGON electrode, implying that the AGON electrode has the larger capacitance.[60] The peak current increases dramatically as the scan rate rises, indicating that the reaction is controlled by the diffusion process. When the scanning rate is increased to 100 mV·s^{-1}, the peak current density does not change significantly, indicating that the rate capability of BGON is relatively weak. The main reason is that the conductivity is limited provided by multi-defect BGO as the substrate. When the scanning rate increased to 100 mV·s^{-1}, its insufficient charge conduction capacity leads to charge accumulation. The electron transfer can be facilitated, and electrochemical performance of the composite material can be improved by the 3D rGO conductive network.

Figure 4c shows the EIS curves and fitting circuit diagram of the two kinds of electrode materials. The fitting results are shown in Table 3. The electrolyte resistance, the intrinsic resistance of the electrode material, and the interface contact resistance are mainly included in R_s.[61] The resistance of CPE and its corresponding n_{CPE} value reflect the capacitance characteristics of materials. When the value of n_{CPE} is closer to 1, the electrochemical performance of materials is closer to an ideal capacitor. The lower CPE impedance of AGON confirms that it has a larger capacity than BGON.[57] The value of n_{CPE} is as high as 0.9, which means that the electrode behavior of AGON is close to an ideal capacitor, which is caused by the AGO as a frame for *in situ* growth of $Ni(OH)_2$ having fewer defects, effectively enhancing the conductivity and reducing the charge accumulation. The charge transfer resistance (R_{ct}) is reflected in the diameter of the semicircle in the high frequency region. The R_{ct} value of AGON is 0.64 Ω, lower than BGON, which further proves that AGON has better conductivity.[62] According to XRD and EIS results, AGO has more sp^2 hybridization carbon atoms leading to excellent conductivity, which makes a decrease in the impedance of AGON and better electrochemical performance. Combined with a larger specific surface area of BGON and images of SEM and TEM, there should be a larger electrode−electrolyte contact area of BGON, but its capacitance and rate capability are the weaker ones. After electrochemical characterization and analysis, it can be concluded that BGON has higher internal resistance. Therefore, the low electron transmission efficiency caused by more defects in the conductive substrate has become an important factor affecting the electrochemical performance of BGON.

Table 3. EIS Parameters and Fitted Values of AGON and BGON at OCP

fitting parameters	AGON	BGON
R_s (Ω)	0.83	0.60
CPE (Ω)	0.005	0.03
n_{CPE}	0.90	0.74
R_{ct} (Ω)	0.64	8.28
W (Ω)	1.54	8.81
n	0.43	0.45

The GCD curves of the two kinds of composites at 2 A·g^{-1} are shown in Figure 4d. The discharging curve of AGON maintains a higher platform of about 0.33 V and lasts longer, corresponding to the less voltage loss for its tiny internal resistance consistent with the EIS analysis.

Figure 4e and Figure 4f show the GCD results of AGON and BGON at different discharge rates, respectively. Both AGON and BGON have visible discharge platforms as current density increases, and the shapes of the discharge curve are similar. Figure 4g exhibits that the C_m values of AGON estimated from the GCD curve are up to 2776 F·g^{-1} at 2 A·g^{-1} and 1570 F·g^{-1} at 50 A·g^{-1} with a high capacity retention rate of nearly 60%. On the contrary, the C_m values of BGON are 1748 F·g^{-1} at 2 A·g^{-1} and 480 F·g^{-1} at 50 A·g^{-1}, and the capacity retention rate was only 27.5%. Both composite materials successfully constructed nanosized $Ni(OH)_2$ sheets and grew them on rGO. Because there are more defects in the rGO of BGON, the corresponding composite materials cannot form an optimally conductive network. Therefore, the BGON electrode has larger internal resistance and lower capacity.

An ASC was assembled utilizing the AGON as the positive electrode. The ASC stores an energy density of 39.24 Wh·kg^{-1} at 1962 W·kg^{-1}. Figure 4h shows the cycle performance of the ASC. The ASC shows a stable cycle performance and retains 91.4% of its initial capacity after 10,000 cycles. The CV curve of the asymmetric capacitor is shown in the inset of Figure 4h, which indicates that the device stores energy by redox reaction.

The insets in Figure 4h are the GCD curves of the ASC for the initial and last five cycles. The curves are consistent and symmetrical, indicating that the ASC has excellent charge−discharge efficiency. The electrochemical polarization of the ASC significantly was reduced, and the charge−discharge platform was inconspicuous, benefiting from the excellent electronic conductivity of the composite electrode. This work shows better stability and rate capability than the results previously reported, as shown in Table 4.

4. CONCLUSIONS

To summarize, two kinds of GO were used as substrates to prepare the NHG composite materials by the hydrothermal method. The results showed that the distribution of $Ni(OH)_2$ in AGON that had better electronic conductivity was not as homogeneous as that in BGON. The C_m of the AGON electrode was up to 2776 F·g^{-1} at 2 A·g^{-1}, which remained 1570 F·g^{-1} at 50 A·g^{-1}. The AGON had a lower charge transfer resistance proven by EIS analysis. Meanwhile, as a result of the improvement of conductivity and the reduction of internal resistance, the discharging platform of AGON is also

https://doi.org/10.1021/acsanm.2c01464
ACS Appl. Nano Mater. 2022, 5, 7471−7480

Table 4. Electrochemical Performance Comparison of This Work and Related Literature

electrode materials	synthesis method	specific capacitance ($F\ g^{-1}$ at $A\ g^{-1}$)	rate capability ($F\ g^{-1}$ at $A\ g^{-1}$)	the capacity retention of the ASC (cycles)	references
G/rGO/$Ni(OH)_2$	*in situ* reaction	1510 at 2	890 at 40	82% (5000th)	63
$Ni(OH)_2$/NG	hydrothermal	896 at 0.5	504 at 12	74.3% (5000th)	34
rGO/α-$Ni(OH)_2$@nickel	dip-coating	2118 at 1	1584 at 10	86.1% (10,000th)	64
$Ni(OH)_2$@GCA	chemical bath deposition	1208 at 1	833.5 at 10	88% (2000th)	65
$Ni(OH)_2$/af-GQDs	hydrothermal	2653 at 1	1658 at 20	90.15% (3000th)	66
NiFe LDHs/rGO/NF	electrodeposition	1462.5 at 5	1053 at 30	64.7% (2000th)	35
β-$Ni(OH)_2$@acid-treated	hydrothermal	1568 at 1	800 at 20	80.8% (3000th)	67
NiO/$Ni(OH)_2$(HTC/NiO/$Ni(OH)_2$@NF)	hydrothermal	2586 at 2.8	1810 at 5.6	91.3% (20,000th)	68
$Ni(OH)_2$/g-C_3N_4/RGO	hydrothermal	543.8 at 1	353.6 at 10	72.7% (2000th)	69
Co_2SiO_4@$Ni(OH)_2$	hydrothermal	1101 at 1	658 at 10	46% (4000th)	70
β-$Ni(OH)_2$/rGO	hydrothermal	2776 at 2	1570 at 50	90.4% (2000th)	this work

increased. Shortening the transport distance of protons in the material, exposing more reaction sites, and enlarging the electrode−electrolyte reaction interface are all advantages of nanosized $Ni(OH)_2$. By growing $Ni(OH)_2$ *in situ* on the 3D conductive network produced by rGO, the electron transfer rate of the AGON composite can be significantly increased, resulting in improved rate capability. BGON has more defects in the carbon network and cannot export electrons effectively. When the power density of the ASC was up to 1962 $W{\cdot}kg^{-1}$, the ASC stored a high energy density of 39.24 $Wh{\cdot}kg^{-1}$. After 10,000 cycles, 91.4% of the initial capacity was preserved by the ASC, demonstrating outstanding cycle performance.

These encouraging findings provide a basis for the subsequent preparation of metal hydroxide/rGO composites, pointing out a direction for the preparation of few-defect/defect-free and highly conductive composites. Most of the works focused on electrochemically active materials after clarifying the role of graphene and its derivatives in composites. Various functional groups on the surface of the substrate material can guide the growth of the active material and produce different distributions, and the substrate defects will also produce different changes in different treatment processes, thus affecting the properties of the composite. Therefore, the physical and chemical properties and functions of the substrate material should be paid more attention to.

■ AUTHOR INFORMATION

Corresponding Author

Meicheng Li − *State Key Laboratory of Alternate Electrical Power System with Renewable Energy Sources, School of New Energy, North China Electric Power University, Beijing 102206, China*; orcid.org/0000-0002-0731-741X; Email: mcli@ncepu.edu.cn

Authors

Binglin Guo − *State Key Laboratory of Alternate Electrical Power System with Renewable Energy Sources, School of New Energy, North China Electric Power University, Beijing 102206, China*

Yihao Gao − *State Key Laboratory of Alternate Electrical Power System with Renewable Energy Sources, School of New Energy, North China Electric Power University, Beijing 102206, China*

Yongyue Li − *State Key Laboratory of Alternate Electrical Power System with Renewable Energy Sources, School of New Energy, North China Electric Power University, Beijing 102206, China*

Xin Sun − *State Key Laboratory of Alternate Electrical Power System with Renewable Energy Sources, School of New Energy, North China Electric Power University, Beijing 102206, China*

Shuailin Chen − *State Key Laboratory of Alternate Electrical Power System with Renewable Energy Sources, School of New Energy, North China Electric Power University, Beijing 102206, China*

Complete contact information is available at: https://pubs.acs.org/10.1021/acsanm.2c01464

Notes

The authors declare no competing financial interest.

■ ACKNOWLEDGMENTS

This work is supported partially by the project of the State Key Laboratory of Alternate Electrical Power System with Renewable Energy Sources (LAPS21004 and LAPS202114), National Natural Science Foundation of China (grant nos. 51972110, 52102245, and 52072121), Beijing Science and Technology Project (Z211100004621010), Beijing Natural Science Foundation (2222076 and 2222077), Huaneng Group Headquarters Science and Technology Project (HNKJ20-H88), the Fundamental Research Funds for the Central Universities (2021MS028, 2020MS023, and 2020MS028), and the NCEPU "Double First-Class" Program.

■ REFERENCES

(1) Wei, W.; Chen, Z.; Zhang, Y.; Chen, J.; Wan, L.; Du, C.; Xie, M.; Guo, X. Full-Faradaic-Active Nitrogen Species Doping Enables High-Energy-Density Carbon-Based Supercapacitor. *J. Energy Chem.* **2020**, *48*, 277−284.

(2) Li, W.; Liu, Y. Y.; Bai, Y.; Wang, J.; Pang, H. Anchoring ZIF-67 Particles on Amidoximerized Polyacrylonitrile Fibers for Radionuclide Sequestration in Wastewater and Seawater. *J. Hazard. Mater.* **2020**, *395*, 122692.

(3) Liang, J.; Qu, T.; Kun, X.; Zhang, Y.; Chen, S.; Cao, Y.-C.; Xie, M.; Guo, X. Microwave Assisted Synthesis of Camellia Oleifera Shell-Derived Porous Carbon with Rich Oxygen Functionalities and Superior Supercapacitor Performance. *Appl. Surf. Sci.* **2018**, *436*, 934−940.

(4) Bo, X.; Xiang, K.; Zhang, Y.; Shen, Y.; Chen, S.; Wang, Y.; Xie, M.; Guo, X. Microwave-Assisted Conversion of Biomass Wastes to Pseudocapacitive Mesoporous Carbon for High-Performance Supercapacitor. *J. Energy Chem.* **2019**, *39*, 1−7.

(5) Han, X. G.; Funk, M. R.; Shen, F.; Chen, Y. C.; Li, Y. Y.; Campbell, C. J.; Dai, J. Q.; Yang, X. F.; Kim, J. W.; Liao, Y. L.; Connell, J. W.; Barone, V.; Chen, Z. F.; Lin, Y.; Hu, L. B. Scalable Holey Graphene Synthesis and Dense Electrode Fabrication toward High-Performance Ultracapacitors. *ACS Nano* **2014**, *8*, 8255−8265.
(6) Zhang, Y.; Cheng, L.; Zhang, L.; Yang, D.; Du, C.; Wan, L.; Chen, J.; Xie, M. Effect of Conjugation Level on the Performance of Porphyrin Polymer Based Supercapacitors. *Journal of Energy Storage* **2021**, *34*, 102018.
(7) Zheng, S.; Sun, Y.; Xue, H.; Braunstein, P.; Huang, W.; Pang, H. Dual-Ligand and Hard-Soft-Acid-Base Strategies to Optimize Metal-Organic Framework Nanocrystals for Stable Electrochemical Cycling Performance. *Natl. Sci. Rev.* **2021**, nwab197.
(8) Zheng, S.; Li, Q.; Xue, H.; Pang, H.; Xu, Q. A Highly Alkaline-Stable Metal Oxide@Metal-Organic Framework Composite for High-Performance Electrochemical Energy Storage. *Natl. Sci. Rev.* **2020**, *7*, 305−314.
(9) Yu, F.; Pang, L.; Wang, H. X. Preparation of Mulberry-Like RuO_2 Electrode Material for Supercapacitors. *Rare Met.* **2021**, *40*, 440−447.
(10) Sari, F. N. I.; So, P. R.; Ting, J. M. MnO_2 with Controlled Phase for Use in Supercapacitors. *J. Am. Ceram. Soc.* **2017**, *100*, 1642−1652.
(11) Hu, Q. Q.; Gu, Z. X.; Zheng, X. T.; Zhang, X. J. Three-Dimensional Co_3O_4@NiO Hierarchical Nanowire Arrays for Solid-State Symmetric Supercapacitor with Enhanced Electrochemical Performances. *Chem. Eng. J.* **2016**, *304*, 223−231.
(12) Bai, Y.; Liu, C.; Chen, T.; Li, W.; Zheng, S.; Pi, Y.; Luo, Y.; Pang, H. MXene-Copper/Cobalt Hybrids via Lewis Acidic Molten Salts Etching for High Performance Symmetric Supercapacitors. *Angew. Chem.* **2021**, *60*, 25318−25322.
(13) Jiang, R.; Da, Y.; Han, X.; Chen, Y.; Deng, Y.; Hu, W. Ultrafast Synthesis for Functional Nanomaterials. *Cell Reports Physical Science* **2021**, *2*, 100302.
(14) Wu, H.; Lu, Q.; Zhang, J.; Wang, J.; Han, X.; Zhao, N.; Hu, W.; Li, J.; Chen, Y.; Deng, Y. Thermal Shock-Activated Spontaneous Growing of Nanosheets for Overall Water Splitting. *Nanomicro Lett* **2020**, *12*, 162.
(15) Dou, S.; Xu, J.; Cui, X.; Liu, W.; Zhang, Z.; Deng, Y.; Hu, W.; Chen, Y. High-Temperature Shock Enabled Nanomanufacturing for Energy-Related Applications. *Adv. Energy Mater.* **2020**, *10*, 2001331.
(16) Xie, M.; Duan, S.; Shen, Y.; Fang, K.; Wang, Y.; Lin, M.; Guo, X. In-Situ-Grown $Mg(OH)_2$-Derived Hybrid α-$Ni(OH)_2$ for Highly Stable Supercapacitor. *ACS Energy Lett.* **2016**, *1*, 814−819.
(17) Cui, B.; Liu, C.; Zhang, J.; Lu, J.; Liu, S.; Chen, F.; Zhou, W.; Qian, G.; Wang, Z.; Deng, Y.; Chen, Y.; Hu, W. Waste to Wealth: Defect-Rich Ni-Incorporated Spent $LiFePO_4$ for Efficient Oxygen Evolution Reaction. *Sci. China Mater.* **2021**, *64*, 2710−2718.
(18) Li, W.; Guo, X.; Geng, P.; Du, M.; Jing, Q.; Chen, X.; Zhang, G.; Li, H.; Xu, Q.; Braunstein, P.; Pang, H. Rational Design and General Synthesis of Multimetallic Metal-Organic Framework Nano-Octahedra for Enhanced Li-S Battery. *Adv. Mater.* **2021**, *33*, No. e2105163.
(19) Okubo, M.; Hosono, E.; Kim, J.-D.; Enomoto, M.; Kojima, N.; Kudo, T.; Zhou, H.; Honma, I. Nanosize Effect on High-Rate Li-Ion Intercalation in $LiCoO_2$ Electrode. *J. Am. Chem. Soc.* **2007**, *129*, 7444−7452.
(20) Shin, J. Y.; Samuelis, D.; Maier, J. Sustained Lithium-Storage Performance of Hierarchical, Nanoporous Anatase TiO_2 at High Rates: Emphasis on Interfacial Storage Phenomena. *Adv. Funct. Mater.* **2011**, *21*, 3464−3472.
(21) Xia, Y.; Mathis, T. S.; Zhao, M. Q.; Anasori, B.; Dang, A.; Zhou, Z.; Cho, H.; Gogotsi, Y.; Yang, S. Thickness-Independent Capacitance of Vertically Aligned Liquid-Crystalline MXenes. *Nature* **2018**, *557*, 409−412.
(22) Dai, X.; Chen, D.; Fan, H. Q.; Zhong, Y.; Chang, L.; Shao, H. B.; Wang, J. M.; Zhang, J. Q.; Cao, C.-N. $Ni(OH)_2$/NiO/Ni Composite Nanotube Arrays for High-Performance Supercapacitors. *Electrochim. Acta* **2015**, *154*, 128−135.
(23) Xie, M.; Xu, Z.; Duan, S.; Tian, Z.; Zhang, Y.; Xiang, K.; Lin, M.; Guo, X.; Ding, W. Facile Growth of Homogeneous $Ni(OH)_2$ Coating on Carbon Nanosheets for High-Performance Asymmetric Supercapacitor Applications. *Nano Res.* **2018**, *11*, 216−224.
(24) Hall, D. S.; Lockwood, D. J.; Bock, C.; MacDougall, B. R. Nickel Hydroxides and Related Materials: a Review of their Structures, Synthesis and Properties. *Proc. R. Soc. A* **2015**, *471*, 20140792.
(25) Shi, X.; Key, J.; Ji, S.; Linkov, V.; Liu, F.; Wang, H.; Gai, H.; Wang, R. $Ni(OH)_2$ Nanoflakes Supported on 3D Ni_3Se_2 Nanowire Array as Highly Efficient Electrodes for Asymmetric Supercapacitor and Ni/MH Battery. *Small* **2019**, *15*, 1802861.
(26) Wang, X.; Song, H.; Ma, S.; Li, M.; He, G.; Xie, M.; Guo, X. Template Ion-Exchange Synthesis of Co-Ni Composite Hydroxides Nanosheets for Supercapacitor with Unprecedented Rate Capability. *Chem. Eng. J.* **2022**, *432*, 134319.
(27) Wang, Y.; Zhang, X.; Li, X.; Li, X.; Zhao, Y.; Wei, H.; Liu, Y.; Jiang, P.; Liang, M. Highly Dispersed Ultrasmall $Ni(OH)_2$ Aggregated Particles on a Conductive Support as a Supercapacitor Electrode with Superior Performance. *J. Colloid Interface Sci.* **2017**, *490*, 252−258.
(28) Gallagher, K. G.; Trask, S. E.; Bauer, C.; Woehrle, T.; Lux, S. F.; Tschech, M.; Lamp, P.; Polzin, B. J.; Ha, S.; Long, B.; Wu, Q.; Lu, W.; Dees, D. W.; Jansen, A. N. Optimizing Areal Capacities through Understanding the Limitations of Lithium-Ion Eectrodes. *J. Electrochem. Soc.* **2016**, *163*, A138−A149.
(29) Zhang, C.; Chen, Q.; Zhan, H. Supercapacitors Based on Reduced Graphene Oxide Nanofibers Supported $Ni(OH)_2$ Nanoplates with Enhanced Electrochemical Performance. *ACS Appl. Mater. Interfaces* **2016**, *8*, 22977−22987.
(30) Liu, T.; Jiang, C.; Cheng, B.; You, W.; Yu, J. Hierarchical Flower-Like C/NiO Composite Hollow Microspheres and its Excellent Supercapacitor Performance. *J. Power Sources* **2017**, *359*, 371−378.
(31) Dong, B.; Li, W.; Huang, X.; Ali, Z. S.; Zhang, T.; Yang, Z.; Hou, Y. Fabrication of Hierarchical Hollow Mn Doped $Ni(OH)_2$ Nanostructures with Enhanced Catalytic Activity towards Electrochemical Oxidation of Methanol. *Nano Energy* **2019**, *55*, 37−41.
(32) Peng, Y.-Y.; Liu, Y.-M.; Chang, J.-K.; Wu, C.-H.; Ger, M.-D.; Pu, N.-W.; Chang, C.-L. A Facile Approach to Produce Holey Graphene and Its Application in Supercapacitors. *Carbon* **2015**, *81*, 347−356.
(33) Yan, J.; Liu, J.; Fan, Z.; Wei, T.; Zhang, L. High-Performance Supercapacitor Electrodes Based on Highly Corrugated Graphene Sheets. *Carbon* **2012**, *50*, 2179−2188.
(34) Li, J.; Hao, H.; Wang, J.; Li, W.; Shen, W. Hydrogels that Couple Nitrogen-Enriched Graphene with $Ni(OH)_2$ Nanosheets for High-Performance Asymmetric Supercapacitors. *J. Alloys Compd.* **2019**, *782*, 516−524.
(35) Li, M.; Jijie, R.; Barras, A.; Roussel, P.; Szunerits, S.; Boukherroub, R. NiFe Layered Double Hydroxide Electrodeposited on Ni Foam Coated with Reduced Graphene Oxide for High-Performance Supercapacitors. *Electrochim. Acta* **2019**, *302*, 1−9.
(36) Lai, L.; Li, R.; Su, S.; Zhang, L.; Cui, Y.; Guo, N.; Shi, W.; Zhu, X. Controllable Synthesis of Reduced Graphene Oxide/Nickel Hydroxide Composites with Different Morphologies for High Performance Supercapacitors. *J. Alloys Compd.* **2020**, *820*, 153120.
(37) Mai, L. Q.; Minhas-Khan, A.; Tian, X.; Hercule, K. M.; Zhao, Y. L.; Lin, X.; Xu, X. Synergistic interaction between redox-active electrolyte and binder-free functionalized carbon for ultrahigh supercapacitor performance. *Nat. Commun.* **2013**, *4*, 2923.
(38) Chen, D.; Feng, H.; Li, J. Graphene Oxide: Preparation, Functionalization, and Electrochemical Applications. *Chem. Rev.* **2012**, *112*, 6027−6053.
(39) Yoo, B. M.; Shin, H. J.; Yoon, H. W.; Park, H. B. Graphene and Graphene Oxide and their Uses in Barrier Polymers. *J. Appl. Polym. Sci.* **2014**, *131*, 39628.
(40) Compton, O. C.; Nguyen, S. T. Graphene Oxide, Highly Reduced Graphene Oxide, and Graphene: Versatile Building Blocks for Carbon-Based Materials. *Small* **2010**, *6*, 711−723.

https://doi.org/10.1021/acsanm.2c01464
ACS Appl. Nano Mater. 2022, 5, 7471−7480

(41) Mkhoyan, K. A.; Contryman, A. W.; Silcox, J.; Stewart, D. A.; Eda, G.; Mattevi, C.; Miller, S.; Chhowalla, M. Atomic and Electronic Structure of Graphene-Oxide. *Nano Lett.* **2009**, *9*, 1058−1063.
(42) Zuo, X.; He, S.; Li, D.; Peng, C.; Huang, Q.; Song, S.; Fan, C. Graphene Oxide-Facilitated Electron Transfer of Metalloproteins at Electrode Surfaces. *Langmuir* **2010**, *26*, 1936−1939.
(43) Mao, Y.; Xie, J.; Liu, H.; Hu, W. Hierarchical Core-Shell Ag@$Ni(OH)_2$@PPy Nanowire Electrode for Ultrahigh Energy Density Asymmetric Supercapacitor. *Chem. Eng. J.* **2021**, *405*, 126984.
(44) Xu, L.; Chen, H.; Shu, K. $Ni(OH)_2$/RGO Nanosheets Constituted 3D Structure for High-Performance Supercapacitors. *J. Sol-Gel Sci. Technol.* **2016**, *77*, 463−469.
(45) Tan, X.; Li, Y.; Li, X.; Zhou, S.; Fan, L.; Yang, S. Electrochemical Synthesis of Small-Sized Red Fluorescent Graphene Quantum Dots as a Bioimaging Platform. *Chem. Commun.* **2015**, *51*, 2544−2546.
(46) Yoon, S. B.; Chai, G. S.; Kang, S. K.; Yu, J. S.; Gierszal, K. P.; Jaroniec, M. Graphitized Pitch-Based Carbons with Ordered Nanopores Synthesized by Using Colloidal Crystals as Templates. *J. Am. Chem. Soc.* **2005**, *127*, 4188−4189.
(47) Sun, L.; Tian, C.; Fu, Y.; Yang, Y.; Yin, J.; Wang, L.; Fu, H. Nitrogen-Doped Porous Graphitic Carbon as an Excellent Electrode Material for Advanced Supercapacitors. *Chemistry-a European Journal* **2014**, *20*, 564−574.
(48) Elias, D. C.; Nair, R. R.; Mohiuddin, T. M. G.; Morozov, S. V.; Blake, P.; Halsall, M. P.; Ferrari, A. C.; Boukhvalov, D. W.; Katsnelson, M. I.; Geim, A. K.; Novoselov, K. S. Control of Graphene's Properties by Reversible Hydrogenation: Evidence for Graphane. *Science* **2009**, *323*, 610−613.
(49) Eda, G.; Mattevi, C.; Yamaguchi, H.; Kim, H.; Chhowalla, M. Insulator to Semimetal Transition in Graphene Oxide. *J. Phys. Chem. C* **2009**, *113*, 15768−15771.
(50) Gomez-Navarro, C.; Weitz, R. T.; Bittner, A. M.; Scolari, M.; Mews, A.; Burghard, M.; Kern, K. Electronic Transport Properties of Individual Chemically Reduced Graphene Oxide Sheets. *Nano Lett.* **2007**, *7*, 3499−3503.
(51) Xu, C.; Wang, X.; Zhu, J. Graphene-Metal Particle Nanocomposites. *J. Phys. Chem. C* **2008**, *112*, 19841−19845.
(52) Zhang, S.; Shao, Y.; Liao, H.-G.; Liu, J.; Aksay, I. A.; Yin, G.; Lin, Y. Graphene Decorated with PtAu Alloy Nanoparticles: Facile Synthesis and Promising Application for Formic Acid Oxidation. *Chem. Mater.* **2011**, *23*, 1079−1081.
(53) Fu, T.; Li, Z. Review of Recent Development in Co-Based Catalysts Supported on Carbon Materials for Fischer-Tropsch Synthesis. *Chem. Eng. Sci.* **2015**, *135*, 3−20.
(54) Bae, G.; Youn, D. H.; Han, S.; Lee, J. S. The Role of Nitrogen in a Carbon Support on The Increased Activity and Stability of a Pt Catalyst in Electrochemical Hydrogen Oxidation. *Carbon* **2013**, *51*, 274−281.
(55) Zhang, H.; Zhang, X.; Zhang, D.; Sun, X.; Lin, H.; Wang, C.; Ma, Y. One-Step Electrophoretic Deposition of Reduced Graphene Oxide and $Ni(OH)_2$ Composite Films for Controlled Syntheses Supercapacitor Electrodes. *J. Phys. Chem. B* **2013**, *117*, 1616−1627.
(56) Cai, F.-S.; Zhang, G.-Y.; Chen, J.; Gou, X.-L.; Liu, H.-K.; Dou, S.-X. $Ni(OH)_2$ Tubes with Mesoscale Dimensions as Positive-Electrode Materials of Alkaline Rechargeable Batteries. *Angewandte Chemie-International Edition* **2004**, *43*, 4212−4216.
(57) Upadhyay, K. K.; Bundaleska, N.; Abrashev, M.; Bundaleski, N.; Teodoro, O. M. N. D.; Fonseca, I.; de Ferro, A. M.; Silva, R. P.; Tatarova, E.; Montemor, M. F. Free-Standing N-Graphene as Conductive Matrix for $Ni(OH)_2$ Based Supercapacitive Electrodes. *Electrochim. Acta* **2020**, *334*, 135592.
(58) Zhao, B.; Zhang, L.; Zhang, Q.; Chen, D.; Cheng, Y.; Deng, X.; Chen, Y.; Murphy, R.; Xiong, X.; Song, B.; Wong, C.-P.; Wang, M.-S.; Liu, M. Rational Design of Nickel Hydroxide-Based Nanocrystals on Graphene for Ultrafast Energy Storage. *Adv. Energy Mater.* **2018**, *8*, 1702247.
(59) Wang, S.; Wang, Z.; Wang, Y.; Chen, J.; Chen, Z.; Chen, Y.; Fu, J. Environmentally Friendly Room Temperature Synthesis of Hierarchical Porous α-$Ni(OH)_2$ Nanosheets for Supercapacitor and Catalysis Applications. *Green Chem.* **2019**, *21*, 5960−5968.
(60) Yi, H.; Wang, H.; Jing, Y.; Peng, T.; Wang, Y.; Guo, J.; He, Q.; Guo, Z.; Wang, X. Advanced Asymmetric Supercapacitors Based on CNT@$Ni(OH)_2$ Core-Shell Composites and 3D Graphene Networks. *J. Mater. Chem. A* **2015**, *3*, 19545−19555.
(61) Wu, Q.; Xu, Y.; Yao, Z.; Liu, A.; Shi, G. Supercapacitors Based on Flexible Graphene/Polyaniline Nanofiber Composite Films. *ACS Nano* **2010**, *4*, 1963−1970.
(62) Cui, B.; Hu, Z.; Liu, C.; Liu, S.; Chen, F.; Hu, S.; Zhang, J.; Zhou, W.; Deng, Y.; Qin, Z.; Wu, Z.; Chen, Y.; Cui, L.; Hu, W. Heterogeneous Lamellar-Edged Fe-$Ni(OH)_2$/Ni_3S_2 Nanoarray for Efficient and Stable Seawater Oxidation. *Nano Res.* **2021**, *14*, 1149−1155.
(63) Tian, J.; Shan, Q.; Yin, X.; Wu, W. A Facile Preparation of Graphene/Reduced Graphene Oxide/$Ni(OH)_2$ Two Dimension Nanocomposites for High Performance Supercapacitors. *Adv. Powder Technol.* **2019**, *30*, 3118−3126.
(64) Lai, L.; Clark, M.; Su, S.; Li, R.; Ivey, D. G.; Zhu, X. Dip-Coating Synthesis of rGO/α-$Ni(OH)_2$@Nickel Foam with Layer-by-Layer Structure for High Performance Binder-Free Supercapacitors. *Electrochim. Acta* **2021**, *368*, 137589.
(65) Fan, W.; Shi, Y.; Gao, W.; Sun, Z.; Liu, T. Graphene-Carbon Nanotube Aerogel with a Scroll-Interconnected-Sheet Structure as an Advanced Framework for A High-Performance Asymmetric Supercapacitor Electrode. *ACS Applied Nano Materials* **2018**, *1*, 4435−4441.
(66) Zheng, L.; Guan, L.; Song, J.; Zheng, H. Rational Design of a Sandwiched Structure $Ni(OH)_2$ Nanohybrid Sustained by Amino-Functionalized Graphene Quantum Dots for Outstanding Capacitance. *Appl. Surf. Sci.* **2019**, *480*, 727−737.
(67) Li, Q.; Lu, C.; Xiao, D.; Zhang, H.; Chen, C.; Xie, L.; Liu, Y.; Yuan, S.; Kong, Q.; Zheng, K.; Yin, J. β-$Ni(OH)_2$ Nanosheet Arrays Grown on Biomass-Derived Hollow Carbon Microtubes for High-Performance Asymmetric Supercapacitors. *ChemElectroChem* **2018**, *5*, 1279−1287.
(68) Zhao, C.; Han, S.; Ding, Y.; Yang, Y.; Jiang, R.; Zhao, C. One-Step Synthesis of Amino Acid-Derived HTC/NiO/$Ni(OH)_2$@Ni Cathode for High Performance Supercapacitors. *Appl. Surf. Sci.* **2021**, *558*, 149853.
(69) Liu, H.; Liu, B.; Sun, X.; Han, X.; Cui, J. L.; Zhang, Y.; He, W. A Simple Hydrothermal Method for the Preparation of 3D Petal-Like $Ni(OH)_2$/g-C_3N_4/RGO Composite with Good Supercapacitor Performance. *Inorg. Chem. Commun.* **2020**, *122*, 108263.
(70) Zhao, Y.; Zhang, Y.; Cheng, Y.; Zhao, W.; Chen, W.; Meng, C.; Huang, C. Synthesis of Co_2SiO_4/$Ni(OH)_2$ Core-Shell Structure as the Supercapacitor Electrode Material with Enhanced Electrochemical Properties. *Mater. Lett.* **2021**, *282*, 128774.

https://doi.org/10.1021/acsanm.2c01464
ACS Appl. Nano Mater. 2022, 5, 7471−7480